Determination of cytoplasmic optineurin foci sizes using image correlation spectroscopy

[1] Laboratory of Molecular Cell Dynamics, Faculty of Advanced Life Science, Hokkaido University, Sapporo, Japan 001-0021
† Corresponding author
Mail: kinjo@sci.hokudai.ac.jp
Tel: +81-11-706-9006 / Fax: +81-11-706-9045

Running title:
Size determination of optineurin foci

Abbreviations
Optineurin: OPTN
Primary open-angle glaucoma: POAG
Amyotrophic lateral sclerosis: ALS
Inclusion body: IB
Image correlation spectroscopy: ICS
Spatial ICS: SICS
Autocorrelation function: ACF
Green fluorescent protein: GFP

Summary

Optineurin (OPTN) plays an important role in membrane trafficking processes such as exocytosis and autophagy. The sizes and rate of formation of accumulated structures comprising OPTN, such as foci or inclusion bodies (IBs), are often disrupted by amyotrophic lateral sclerosis (ALS) and glaucoma-associated mutants of OPTN. Therefore, methods for the quantitative measurement of the size of the accumulated structure are necessary. Here, we show that, using spatial image correlation spectroscopy (ICS), the average diameter of accumulated structures of the wild type and disease-associated mutants in living cells may be easily determined. Although OPTN was found to frequently form foci in the cytoplasm, regardless of ALS- and glaucoma-associated mutation, the diameter of OPTN foci decreased in an ALS-associated mutant and increased in a glaucoma-associated mutant. However, a portion of cells carried IBs of the ALS-associated mutant that were larger than micrometer and ellipse-like shape, suggesting that this mutant accumulates non-uniformly in the IBs. The findings suggest that changes in their accumulation, determined via quantitative comparison of the OPTN foci and IBs in the cells, are involved in pathological features of ALS. In addition, this method enables rapid comparison of the average sizes of various other intracellular structures such as granules.

Keywords

Optineurin; vesicular trafficking; foci; inclusion body; image correlation spectroscopy

Introduction

Vesicular trafficking, which involves endocytosis, exocytosis, and autophagy, is a well-conserved and highly regulated cellular process in eukaryotic cells; this process enables targeted delivery of specific components to selective compartments such as the extracellular space, endosome, and lysosome. Adapter or regulatory proteins play an important role in the efficient delivery of these components. Regulatory proteins temporarily accumulate on vesicular membranes to regulate functions (*1, 2*). When diffusing proteins temporarily attach to the membrane, their localization on vesicles may be observed as foci in the cytoplasm in the autophagosomes, endosomes, and endoplasmic reticulum exit sites. However, misfolded or denatured proteins in the cells often form aggregates that accumulate in the inclusion bodies (IBs) (*3, 4*). The foci and IBs may be observed by optical microscopy as well as electron microscopy; accordingly, the characterization of the foci and IBs via size quantification is a straightforward procedure. However, the measurement of foci diameter individually is complex; therefore, a facile method for the estimation of the diameter of foci and IBs is important.

Fluorescence fluctuation-based methods, such as fluorescence correlation spectroscopy (FCS), image correlation spectroscopy (ICS), and number and brightness (N&B) procedure, are used for various analyses for accumulated proteins in cell biology. In FCS and ICS, temporal and/or spatial correlation functions reflecting molecular size or dynamics are calculated from the recorded fluorescence fluctuation. Specifically, FCS is suitable for measuring the diffusion rate of molecules in living cells and solution (*3, 5*). The N&B procedure enables detection of oligomeric units of aggregates or oligomers (*6*). Importantly, ICS includes two kinds of flexibility: the spatial and temporal persistence of the fluorescence intensity, which correspond to size and residence time of molecules or particles, respectively (*7*). Therefore, ICS is an attractive method for the quantitative determination of the size of the foci or IBs.

Optineurin (OPTN), which is also called as FIP2 or NRP, is a multidomain protein encoded by the *OPTN* gene; this protein comprises several coiled-coil, leucine zipper, zinc finger, and ubiquitin (Ub)-associating region, and mediates various functions by interacting with numerous different proteins. OPTN was initially identified as a regulator of NF-κB and interferon signaling; however, recently, its role in post-Golgi vesicular trafficking and selective autophagy, including mitophagy and xenophagy, has been reported (*8, 9*). Thus, the majority of OPTN foci are autophagosome- or trafficking vesicle-associated (*10-12*).

Mutations in OPTN that lead to amino acid substitutions have been implicated in several genetic diseases: amyotrophic lateral sclerosis (ALS) and primary open-angle glaucoma (POAG) (*9, 13, 14*). From familial ALS patients, Q398X nonsense or E478G missense mutation in *OPTN* gene have been identified (*10*). In motor neurons from patients with sporadic

and familial ALS, Ub- and TDP-43-positive OPTN IBs have been observed (*10*). The ALS-linked Q398X and E478G mutants of OPTN cause defects of vesicular trafficking (*15*). Since the Q398X mutant of OPTN does not efficiently expressed probably because of nonsense-mediated mRNA decay (*10*), aggregation property of the E478G missense mutation lacking binding ability to poly-ubiquitin chain has been investigated. On the other hand, overexpression of the most common E50K mutant of OPTN in POAG leads to progressive retinal degeneration in mice (*16*). In the POAG-linked E50K mutant of OPTN, enlarged foci are often observed (*11, 12, 16*). However, the quantitative size comparison of OPTN foci and IBs has not been reported to date. Therefore, we established an ICS-based procedure to quantitatively compare the diameter of the foci and IBs of the wild type (WT) and disease-associated mutants of OPTN (E50K and E478G).

Material & Methods

Preparation of plasmids coding for GFP-tagged OPTN

The plasmid coding for the complementary cDNA sequence of optineurin (OPTN) was obtained from the MGC collection (BC032762; Thermo Fisher Scientific, Waltham, MA). The cDNA lacks 628–645 bp relative to the splicing variant type 1 of the OPTN transcript (NM_001008211); thus, in order to complement the lacking sequence, double-stranded synthetic oligo (5'-gggcccacgagaacagtctccactggcacggcattgtctaaatataggagcagatct-3') was inserted into the original plasmid via ApaI and BglII restriction sites. A clone carrying the correct sequence was selected using a genetic analyzer (Applied Biosystems, Waltham, MA) and used for PCR as a template, with forward (5'- agcagaattctatgtcccatcaacctctcagctgcctc-3') and reverse (5'- tgctggatcccgaatgatgcaatccatcacgtgaatc-3') primers. The amplified fragments were cut and inserted into the pBluescript II KS(+) vector. The plasmids coding for OPTN with E50K and E478G amino acid substitutions were constructed using the PCR-based mutagenesis method with the following primers: E50K, 5'-gagctcctgaccAagaaccaccagc-3' and 5'-gctggtggttctTggtcaggagctc-3'; E478G, 5'-gattttcatgctgGaagagcagcgag-3' and 5'-ctcgctgctcttCcagcatgaaaatc-3'. In order to construct plasmids coding for green fluorescent protein (GFP)-tagged OPTN, fragments encoding OPTN-WT, -E50K, and -E478G were cut using EcoRI and BamHI, and inserted into the pmeGFP-C1 vector (*5*) (GFP-OPTN-WT, -E50K, and -E478G, respectively).

Cell culture and transfection

Mouse neuroblastoma Neuro2A cells were maintained as previously reported (*5*), and 2.0×10^5 cells were grown in a glass-based dish (#3910-035, Asahi-Techno-glass, Shizuoka, Japan) for 16 h prior to transfection. The plasmid coding for GFP-OPTN (1.0 μg) was transfected into the cells with 2.0 μL of Lipofectamine 2000 (Thermo Fisher Scientific). After incubation of the cells for 24 h, subsequent experiments were performed.

Quantification of efficiency of foci or IB formation

To determine the proportion of the cells containing OPTN foci or IBs, confocal fluorescence images were acquired using an LSM 510 META (Carl Zeiss, Jena, Germany) through a C-Apochromat 40×/1.2NA Korr UV-VIS-IR water-immersion objective (Carl Zeiss). A confocal pinhole diameter was adjusted to 71 μm. GFPs were excited at 488 nm and emission signals were detected using a 505-nm long-pass filter. The zoom factor was 1. The number of cells and cells containing foci or IBs was counted manually.

Spatial ICS (SICS)

Confocal fluorescence images were acquired using an LSM 510 META (Carl Zeiss) through a C-Apochromat 40×/1.2NA Korr UV-VIS-IR water-immersion objective (Carl Zeiss). A confocal pinhole diameter was adjusted to 71 μm. GFPs were excited at 488 nm and emission signals were detected using a 505-nm long-pass filter. The zoom factor was 8 (The pixel size was 55 nm). After the measurement of cytoplasmic background fluorescence intensities (not included foci or IBs), the background was subtracted using ImageJ 1.51j8 (NIH, Bethesda, MD, USA).

The two-dimensional (2D) spatial autocorrelation function (ACF) was defined as Eq. 1:

$$g(\xi,\eta) = \langle \delta i(x,y)\delta i(x+\xi, y+\eta)\rangle \quad (1)$$

with the fluctuation in fluorescence, $\delta i(x, y)$, given by Eq. 2:

$$\delta i(x,y) = i(x,y) - \langle i(x,y)\rangle \quad (2)$$

where $i(x, y)$ is the intensity at pixel (x, y) in the image; ξ and η are the lag pixels for x- and y-direction, respectively; and $\langle i(x,y)\rangle$ is the average intensity of the image. These functions are typically calculated using Fourier transform methods with GNU Octave software version 4.2.1 platform (*17*) (Eq. 3):

$$g(\xi,\eta) = \mathcal{F}^{-1}\left[\mathcal{F}\left(i(x,\ y)\right)\cdot\mathcal{F}^{*}\left(i(x,y)\right)\right] \quad (3)$$

where $\mathcal{F}$ denotes the 2D spatial Fourier transform, $\mathcal{F}^{*}$ is the complex conjugate of this transform, and $\mathcal{F}^{-1}$ is the inverse 2D spatial Fourier transform. To obtain the distribution of the spatial ACF, modified 2D Gaussian function (Eq. 4) was used:

$$g(\xi,\eta) = g_0 + A\cdot\exp\left[-\frac{1}{2}\left(\frac{\xi\cos\theta+\eta\sin\theta-\xi_c\cos\theta-\eta_c\sin\theta}{w_l}\right)^2 - \frac{1}{2}\left(\frac{-\xi\sin\theta+\eta\cos\theta+\xi_c\sin\theta-\eta_c\cos\theta}{w_s}\right)^2\right] \quad (4)$$

where g_0 is the base line; A is the maximum amplitude; ξ_c and η_c are the center coordinates of the 2D distribution for ξ and η-direction, respectively; w_l and w_s are the major and minor standard deviations of the distribution, respectively; θ is the orientation factor. Non-linear fitting analysis and data visualization were performed using Origin Pro 2017 software (Origin Lab., Northampton, MA, USA). Major and minor radii of the foci or IBs were calibrated from w_l and w_s using Eq. 5 modified from linear regression equation (represented in Figure 2D):

$$r_i = \frac{w_i + 0.0647}{0.829} \quad (5)$$

where r_i is the calibrated radii ($i = l$ or s). Average major and minor diameters (d_l and d_s) were doubled r_l and r_s value, respectively.

For demonstration of size determination using SICS, images including dot(s) were generated using ImageJ 1.50i and then modified with Photoshop CC platform (Adobe Systems Incorp., San Jose, CA, USA). Images including random noise were created using a plugin for ImageJ (Salt and Pepper tool).

Data analysis and statistics

Representative images were processed using ImageJ 1.50i (NIH). Student's *t*-tests were performed using MS-Excel in Office 365 ProPlus Ver. 1708 (Microsoft Corp., Redmond, WA, USA). Plots were created using Origin Pro 2017, and their appearance such as color and axis labels was modified using Illustrator CC (Adobe Systems Incorp.).

Results

Cytoplasmic foci or inclusion body formation of GFP-OPTN

Confocal microscopy was used to evaluate the subcellular localization of GFP-OPTN. GFP-OPTN-WT, -E50K, and -E478G were mainly distributed in the cytoplasm, and their abundance in the nucleus was low (Figure 1A). Since various functional analysis using GFP-tagged OPTN has been performed (*18, 19*), there is little influence of GFP tag in the subcellular localization of OPTN. Although almost all cells expressing GFP-OPTN-WT and -E50K carried cytoplasmic foci, the proportion of cells carrying foci of GFP-OPTN-E50K was slightly higher than that carrying WT (Figure 1B). The fluorescence intensity of the foci of the E50K mutant was brighter than that of WT (Figure 1A); this may be attributed to the accumulation of high levels of the E50K mutant of OPTN in the foci. The proportion of cells carrying foci of GFP-OPTN-E478G was decreased, which agreed with the findings of previous reports (*10, 12*)

(Figure 1B); however, a proportion of cells expressing GFP-OPTN-E478G (5.8%) exhibited enlarged cytoplasmic structure (> 2 μm as a diameter) that shows extremely high fluorescence intensity compared with the WT and E50K mutant (Figure 1A, white arrow; Figure 1C). As intracytoplasmic IBs have been identified in motor neurons form patients with ALS (*10*), the enlarged structure of E478G mutant was defined as an IB. These results suggest that the disease-associated mutant of OPTN may exhibit altered accumulation in the cytoplasm. Therefore, we subsequently attempted to quantitatively measure the size of foci or IBs.

Circle size measurement using SICS

In order to determine the dot size using SICS, we constructed images containing circle(s) or dots with known radii (0.5, 2.5, 5, 7.5, 10 pixels) by image processing (Figure 2A, a–g). The SICS images obtained from single-circle image showed strong amplitude at the center of the image (Figure 2A, h–k). The SICS images calculated from images in which circles were regularly arranged showed not only strong amplitude at the center of the image but also ordered spread patterns according to the original circle arrangement (Figure 2A, l–m). As the SICS image was calculated from the image containing randomly arranged dots (Figure 2A, n), the ordered spread pattern in SICS image reflected the ordered arrangement of structures in the original image.

To analyze average size of the circles in the original images, the center region in the SICS image was cropped (Figure 2B, a and b); then, non-linear fitting was performed using the 2D Gaussian function (Eq. 4; Figure 2B, c and d). The fitted function successfully corresponded to the intensity distribution of the original circle; however, the obtained w value when using Eq. 4 (also known as the standard deviation of the Gaussian distribution) represents the distance from the distribution center at the position at which the maximum peak of the Gaussian function decreases $e^{-0.5}$ times, and therefore does not represent the radius of the circle (Figure 2C). Therefore, in order to determine the radius of the circle, we obtained a calibration formula between real radii of the circles and fitted w values using linear regression analysis (Figure 2D). Using the calibration formula, the radii of the circles were successfully obtained with an error of less than 0.2 pixels (Figure 2E). Therefore, using SICS, the mean radius of foci in the cells may be determined.

Measurement of OPTN foci or IBs using SICS in living cells

To quantitatively determine the shape of the foci or IBs of OPTN, we adopted SICS analysis. As shown in the previous section and Figure 2, SICS analysis is able to determine the radius of the structure in the image. However, the center peak of spatial ACF was dramatically affected by the fluorescence intensity distribution of GFP-OPTN throughout the cytoplasm

(Supplemental Figure); thus, fluorescence intensity of the cytoplasmic region that did not form foci or IBs was subtracted from the original confocal images; then, SICS analysis was performed (Figure 3A). The spatial ACFs of cells containing OPTN foci showed the distribution of low amplitude in addition to high amplitude at the center (Figure 3A, i–k). The two types of distribution of amplitude may be attributable to the average size of each foci, as well as to the foci being distributed and localized in the cytoplasm with a certain order. In contrast, the spatial ACF of IB of the E478G mutant of OPTN showed only a high peak at the center (Figure 3A, l). This may be attributed to the relatively high fluorescence intensity of the IBs. Moreover, the directionality in which the foci were distributed in the fluorescence image is also reflected in the directionality of the intensity distribution in the spatial ACF (Figure 3A, i–k), suggesting that it would be possible to determine the average space in which foci are distributed in the cytoplasm.

Next, to quantify the distribution of the amplitude at the center in spatial ACF, 2D Gaussian function, including the orientation factor, was employed (Eq. 4; Figure 3B). As the orientation of the cells was not unified during image acquisition, the orientation factor served to increase the accuracy of fitting the Gaussian function to the distribution of the peaks in spatial ACF. Using calculated major and minor standard deviations from the fitting and calibrated function obtained in Figure 2D, the average major and minor diameters (d_l and d_s, respectively) of the foci and IBs of GFP-OPTN in living cells were determined. Both the d_l and d_s of foci of GFP-OPTN-E50K were longer than that of the WT and E478G mutant (Figure 3C). The d_l and d_s of foci of the E478G mutant showed a tendency to be short (Figure 3C), suggesting that this mutant may be difficult to assemble compared with WT. The d_l and d_s of IBs of the E478G mutant were dramatically longer than the foci (Figure 3C), suggesting that the IBs may contain large amounts of OPTN compared with the foci.

The ratio between the d_l and d_s of the foci showed an increasing tendency (Figure 3D); this was considered to occur because a portion of the foci was adjoined, even though the shape of the foci was almost uniform. Moreover, a proportion of the IBs of the E478G mutant showed a large ratio between d_l and d_s, and there were few cases where the ratio showed values close to 1 (Figure 3D), suggesting that the shape of the IBs of the E478G mutant may not be a uniform sphere.

Discussion

In the present work, we established a spatial fluorescence fluctuation-based procedure to determine the average size of intracytoplasmic foci or IBs of OPTN in cells. The procedure may be adapted to other proteins that form granules, foci, or IBs, in fixed or living cells. The method additionally enables the quantitative comparison of the sizes of foci and IBs in a facile and rapid manner. In particular, it is effective for rapid determination of average size of multiple foci; thus, SICS analysis may be applied to high-throughput detection of the structure and shape

of cells. Using images with dots of known sizes, the accuracy of the radii of the dots determined from SICS analysis was determined to be less than 0.2 pixel (Figure 2). This corresponds to 11 nm in terms of pixel size, as shown in Figure 3. Therefore, the accuracy is sufficient to determine the size at the sub-diffraction limit when using a confocal fluorescence microscope.

OPTN is associated with vesicular trafficking processes such as the maintenance of Golgi apparatus, exocytosis, and autophagy (*9, 13*). Almost all cells expressing OPTN-WT possessed cytoplasmic foci (Figure 1); thus, foci may be involved in vesicular trafficking including autophagy. TBK1, a kinase for OPTN regulation, is known to colocalize with OPTN foci (*11*); thus, the foci are thought to provide an environment suited to effective enzymatic activity in the cytoplasm by facilitating concentration of the proteins.

Almost all cells expressing WT and the E50K mutant of OPTN carried cytoplasmic foci; however, the proportion of cells was decreased in the E478G mutant; in addition, the size of E478G foci tended to be slightly lower than that of the WT. As the E478G mutant binds more weakly to linear (M1)-linked poly-Ub than does the WT (*20*), the decrease in the proportion of the cells carrying the E478G foci may be attributed to the low binding efficiency between OPTN-E478G and the M1-linked Ub chain. Moreover, the E478G foci were not entirely lost, and the E478G mutant of OPTN retained the ability to bind the Lys63 (K63)-linked Ub chain (*20*). K63 chains act as proteasome-independent signals for endocytosis, DNA damage responses, and immune responses (*21*). Therefore, the E478G foci may represent the position of the scaffold associated with signal transduction via the K63-linked Ub chain, and the scaffold size would be smaller than that associated with the M1-linked chain. A proportion of cells expressing E478G mutant harbored structures with extremely large diameter (2.7–3.4 μm). The IBs of OPTN in motor neurons from patients with ALS colocalize with Ub and TDP-43 aggregates, even though the E478G mutant does not bind the M1-linked Ub chain. Hence, OPTN in the IBs may be misfolded, and the IBs are considered to sequestrate several protein aggregates.

The diameter of the E50K foci was enlarged (1.2–1.3 μm); however, these foci were dramatically smaller than the IBs of the E478G mutant. The E50K mutation altered the oligomeric state of OPTN and induced its tetramerization (*11*). The enlargement of the E50K foci may occur because the oligomeric OPTN efficiently sequestrates several OPTN-binding proteins such as LC3, TBC1D17, and TBK1 (*11, 15, 22*).

The increase in the ratio between the d_l and d_s of the foci (Figure 3D) enables the proximity of the OPTN-WT foci to be determined. As OPTN is involved in vesicular trafficking and mitophagy in the cytoplasm (*19, 23*), the intermediate fusion and fission of the membrane vesicle containing OPTN may be visualized. However, individual E478G IBs were observed to possess an ellipse-like shape (Figure 3, C and D), suggesting that misfolded OPTN may accumulate non-uniformly in the IBs. The ellipse-like shape would be involved in the physical properties of aggregates in the IBs such as solid or gel phase. Accordingly, the ALS-associated

E478G mutant and glaucoma-associated E50K mutant of OPTN may possess distinct functions, especially with regard to vesicular trafficking and/or signal transduction. The present method using SICS enables facile determination of the average size of foci such as granules, autophagosomes, endosomes, and other physiological structures in the cell. In future, the function of the foci of OPTN should be clarified in detail.

Acknowledgements

We are grateful to Dr. J. Yamamoto and Mr. R. Fukushima for their assistance with SICS analysis.

Funding

A.K. was supported by the Japan Society for Promotion of Science (JSPS) Grant-in-Aid for the Promotion of Joint International Research (Fostering Joint International Research) (16KK0156); the JSPS Grant-in-Aid for Scientific Research (C) (#26440090); by the Grant-in-Aid of The Nakabayashi Trust for ALS Research (Tokyo, Japan); by the Grant-in-Aid of the Japan Amyotrophic Lateral Sclerosis Association (JALSA, Tokyo, Japan) for ALS research, and by a grant from the Akiyama Life Science Foundation (Sapporo, Japan).

Author contributions

Conceived and designed the experiments: AK. Plasmid construction: AK. Performed the SICS demonstration: AK. Performed the SICS analysis: AK, HS. Analyzed the data: AK, HS, and MK. Figure construction: AK. Wrote the paper: AK and MK.

Conflict of interest

None declared.

References

(1) Kaksonen, M., and Roux, A. (2018) Mechanisms of clathrin-mediated endocytosis. *Nature reviews. Molecular cell biology*.

(2) Witkos, T.M., and Lowe, M. (2017) Recognition and tethering of transport vesicles at the Golgi apparatus. *Current opinion in cell biology*. **47**, 16-23

(3) Kitamura, A., Nagata, K., and Kinjo, M. (2015) Conformational analysis of misfolded protein aggregation by FRET and live-cell imaging techniques. *International journal of molecular sciences*. **16**, 6076-6092

(4) Miller, S.B., Ho, C.T., Winkler, J., Khokhrina, M., Neuner, A., Mohamed, M.Y., Guilbride, D.L., Richter, K., Lisby, M., Schiebel, E., Mogk, A., and Bukau, B. (2015) Compartment-specific aggregases direct distinct nuclear and cytoplasmic aggregate deposition. *The EMBO journal*. **34**, 778-797

(5) Kitamura, A., Nakayama, Y., Shibasaki, A., Taki, A., Yuno, S., Takeda, K., Yahara, M., Tanabe, N., and Kinjo, M. (2016) Interaction of RNA with a C-terminal fragment of the amyotrophic lateral sclerosis-associated TDP43 reduces cytotoxicity. *Scientific reports*. **6**, 19230

(6) Kim, Y.E., Hosp, F., Frottin, F., Ge, H., Mann, M., Hayer-Hartl, M., and Hartl, F.U. (2016) Soluble Oligomers of PolyQ-Expanded Huntingtin Target a Multiplicity of Key Cellular Factors. *Molecular cell*. **63**, 951-964

(7) Kolin, D.L., and Wiseman, P.W. (2007) Advances in image correlation spectroscopy: measuring number densities, aggregation states, and dynamics of fluorescently labeled macromolecules in cells. *Cell biochemistry and biophysics*. **49**, 141-164

(8) Wild, P., Farhan, H., McEwan, D.G., Wagner, S., Rogov, V.V., Brady, N.R., Richter, B., Korac, J., Waidmann, O., Choudhary, C., Dotsch, V., Bumann, D., and Dikic, I. (2011) Phosphorylation of the autophagy receptor optineurin restricts Salmonella growth. *Science*. **333**, 228-233

(9) Slowicka, K., Vereecke, L., and van Loo, G. (2016) Cellular Functions of Optineurin in Health and Disease. *Trends Immunol*. **37**, 621-633

(10) Maruyama, H., Morino, H., Ito, H., Izumi, Y., Kato, H., Watanabe, Y., Kinoshita, Y., Kamada, M., Nodera, H., Suzuki, H., Komure, O., Matsuura, S., Kobatake, K., Morimoto, N., Abe, K., Suzuki, N., Aoki, M., Kawata, A., Hirai, T., Kato, T., Ogasawara, K., Hirano, A., Takumi, T., Kusaka, H., Hagiwara, K., Kaji, R., and Kawakami, H. (2010) Mutations of optineurin in amyotrophic lateral sclerosis. *Nature*. **465**, 223-226

(11) Li, F., Xie, X., Wang, Y., Liu, J., Cheng, X., Guo, Y., Gong, Y., Hu, S., and Pan, L. (2016) Structural insights into the interaction and disease mechanism of neurodegenerative disease-associated optineurin and TBK1 proteins. *Nature communications*. **7**, 12708

(12) Sundaramoorthy, V., Walker, A.K., Tan, V., Fifita, J.A., McCann, E.P., Williams, K.L., Blair,

I.P., Guillemin, G.J., Farg, M.A., and Atkin, J.D. (2015) Defects in optineurin- and myosin VI-mediated cellular trafficking in amyotrophic lateral sclerosis. *Human molecular genetics*. **24**, 3830-3846

(13) Minegishi, Y., Nakayama, M., Iejima, D., Kawase, K., and Iwata, T. (2016) Significance of optineurin mutations in glaucoma and other diseases. *Prog Retin Eye Res*. **55**, 149-181

(14) Bansal, M., Swarup, G., and Balasubramanian, D. (2015) Functional analysis of optineurin and some of its disease-associated mutants. *IUBMB Life*. **67**, 120-128

(15) Sundaramoorthy, V., Walker, A.K., Tan, V., Fifita, J.A., McCann, E.P., Williams, K.L., Blair, I.P., Guillemin, G.J., Farg, M.A., and Atkin, J.D. (2017) Defects in optineurin- and myosin VI-mediated cellular trafficking in amyotrophic lateral sclerosis. *Human molecular genetics*. **26**, 3452

(16) Chi, Z.L., Akahori, M., Obazawa, M., Minami, M., Noda, T., Nakaya, N., Tomarev, S., Kawase, K., Yamamoto, T., Noda, S., Sasaoka, M., Shimazaki, A., Takada, Y., and Iwata, T. (2010) Overexpression of optineurin E50K disrupts Rab8 interaction and leads to a progressive retinal degeneration in mice. *Human molecular genetics*. **19**, 2606-2615

(17) Petersen, N.O., Hoddelius, P.L., Wiseman, P.W., Seger, O., and Magnusson, K.E. (1993) Quantitation of membrane receptor distributions by image correlation spectroscopy: concept and application. *Biophysical journal*. **65**, 1135-1146

(18) Wong, Y.C., and Holzbaur, E.L. (2014) Optineurin is an autophagy receptor for damaged mitochondria in parkin-mediated mitophagy that is disrupted by an ALS-linked mutation. *Proceedings of the National Academy of Sciences of the United States of America*. **111**, E4439-4448

(19) Richter, B., Sliter, D.A., Herhaus, L., Stolz, A., Wang, C., Beli, P., Zaffagnini, G., Wild, P., Martens, S., Wagner, S.A., Youle, R.J., and Dikic, I. (2016) Phosphorylation of OPTN by TBK1 enhances its binding to Ub chains and promotes selective autophagy of damaged mitochondria. *Proceedings of the National Academy of Sciences of the United States of America*. **113**, 4039-4044

(20) Nakazawa, S., Oikawa, D., Ishii, R., Ayaki, T., Takahashi, H., Takeda, H., Ishitani, R., Kamei, K., Takeyoshi, I., Kawakami, H., Iwai, K., Hatada, I., Sawasaki, T., Ito, H., Nureki, O., and Tokunaga, F. (2016) Linear ubiquitination is involved in the pathogenesis of optineurin-associated amyotrophic lateral sclerosis. *Nature communications*. **7**, 12547

(21) Erpapazoglou, Z., Walker, O., and Haguenauer-Tsapis, R. (2014) Versatile roles of k63-linked ubiquitin chains in trafficking. *Cells*. **3**, 1027-1088

(22) Chalasani, M.L., Kumari, A., Radha, V., and Swarup, G. (2014) E50K-OPTN-induced retinal cell death involves the Rab GTPase-activating protein, TBC1D17 mediated block in autophagy. *PloS one*. **9**, e95758

(23) Chen, K., Dai, H., Yuan, J., Chen, J., Lin, L., Zhang, W., Wang, L., Zhang, J., Li, K., and He, Y. (2018) Optineurin-mediated mitophagy protects renal tubular epithelial cells

against accelerated senescence in diabetic nephropathy. *Cell death & disease*. **9**, 105

Figure legends

Figure 1. Formation of cytoplasmic foci or inclusion bodies in GFP-tagged wild-type and glaucoma- or ALS-associated mutant of optineurin

(A) Confocal fluorescence image of typical Neuro2A cells expressing GFP-OPTN-WT, -E50K, and E478G. Cells expressing E478G mutant exhibit two distinct patterns: foci and inclusion body (IB; white arrow); bar = 5 μm. (B) The proportion of cells carrying cytoplasmic foci of GFP-OPTN-WT, -E50K, and -E478G (C) The proportion of cells carrying cytoplasmic IBs of GFP-OPTN-WT, -E50K, and -E478G (B & C) In three trials, the total number of analyzed cells: 59, 74, and 82 for WT; 94, 87, and 117 for E50K; and 125, 44, and 100 for E478G. Bars: mean ± s.e.m (n = 3); Inset numerical value indicates mean. Student's *t*-test: $*p < 0.05$, $**p < 0.01$, and $***p < 0.001$.

Figure 2. Demonstration of circle size measurement using SICS

(A) Original images including dot(s) (a–g) and 2D spatial autocorrelation function (ACF) images using SICS calculation (h–n) are shown. Line and cross indicate images including numerous circles with a radius of 5 pixels, which are drawn with 30 or -30 pixels in the *x* direction around the center and additionally in the *y* direction at the same distance, respectively; bar = 10 pixels. The color scale for the ACF image is shown in the right side of the ACF images. (B) Scheme of SICS analysis a. The ACF image is the same as in m. in (A). b. An image of the cropped center region c. and d. Before and after non-linear fitting analysis using 2D Gaussian function (Eq. 4, see Material & Methods) on Origin 2017, respectively. Color scales are shown at the right side of the ACF images. Contour lines in d. indicates the height of fitted 2D Gaussian function from 0 to 0.85 in 0.05 increments. (C) Overlap of 1D-dropped intensity profile of a circle with 5-pixel radius (green) and Gaussian function when A is 1.0, ξ_c, η_c, θ, η, and g_0 are 0, and standard deviation (w) is 4.02 in Eq. 4 (magenta). The intensity of the original circle was normalized to 0.5. Double arrow indicates the width of w and $e^{-0.5}$. (D) Linear regression analysis between real radii of the circle and fitted w values; inset function indicates the calibration formula (blue line). (E) Fitted w value and calibrated radii of the circles using the Eq. in (D) were shown (light and dark gray, respectively). The inset graph indicates residuals between fitted w values and calibrated radii.

Figure 3. Comparison of the size of foci or inclusion bodies of ALS- and POAG-linked mutant of OPTN using SICS

(A) Confocal fluorescence, cytoplasmic background intensity-subtracted, spatial ACF images are shown. Color scales are indicated at the right side of the images; bar = 5 μm. (B) Top view of 2D Gaussian function (Eq. 4) for the ξ and η coordinates when ξ_c and η_c is 0. w_l and w_s are major and minor standard deviation, respectively. θ is the orientation factor. (C) Major and

minor diameter (d_l and d_s) are plotted (magenta and cyan, respectively). The diameters are twice the calibrated radii from w_l and w_s using the Eq. 5; bars: means ± s.e.m. (n = 10) Inset numerical values indicate means. Student's *t*-test: ***$p < 0.001$. The number sign on E478G (IB) are significance when compared to the others ($p < 0.001$). (D) Ratios of the diameter in each cell are plotted; ns: no significant difference.

Figure 1

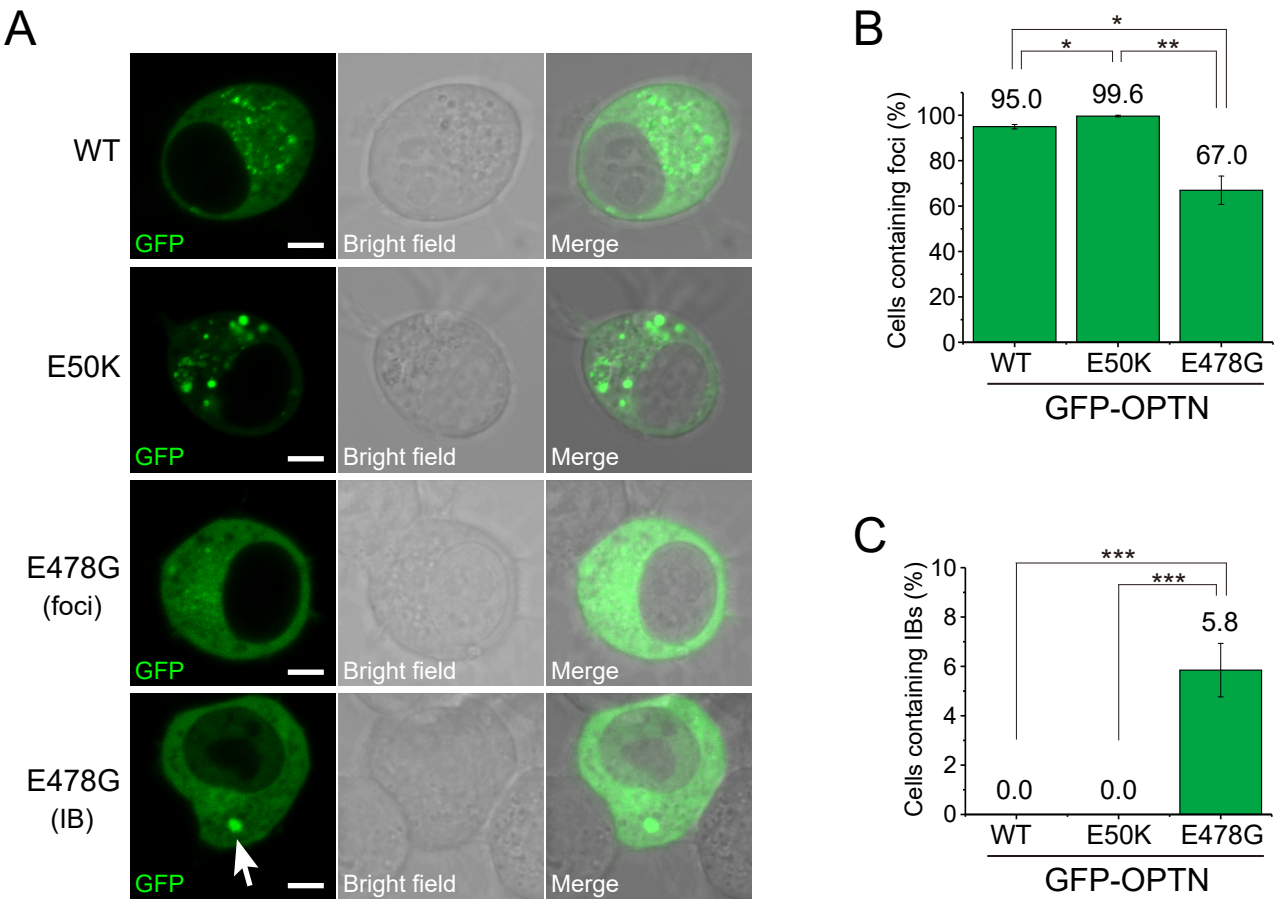
A
WT
E50K
E478G
(foci)
E478G
(IB)
GFP
Bright field
Merge
B
Cells containing foci (%)
95.0
99.6
67.0
WT
E50K
E478G
GFP-OPTN
C
Cells containing IBs (%)
0.0
0.0
5.8
WT
E50K
E478G
GFP-OPTN

Figure 2

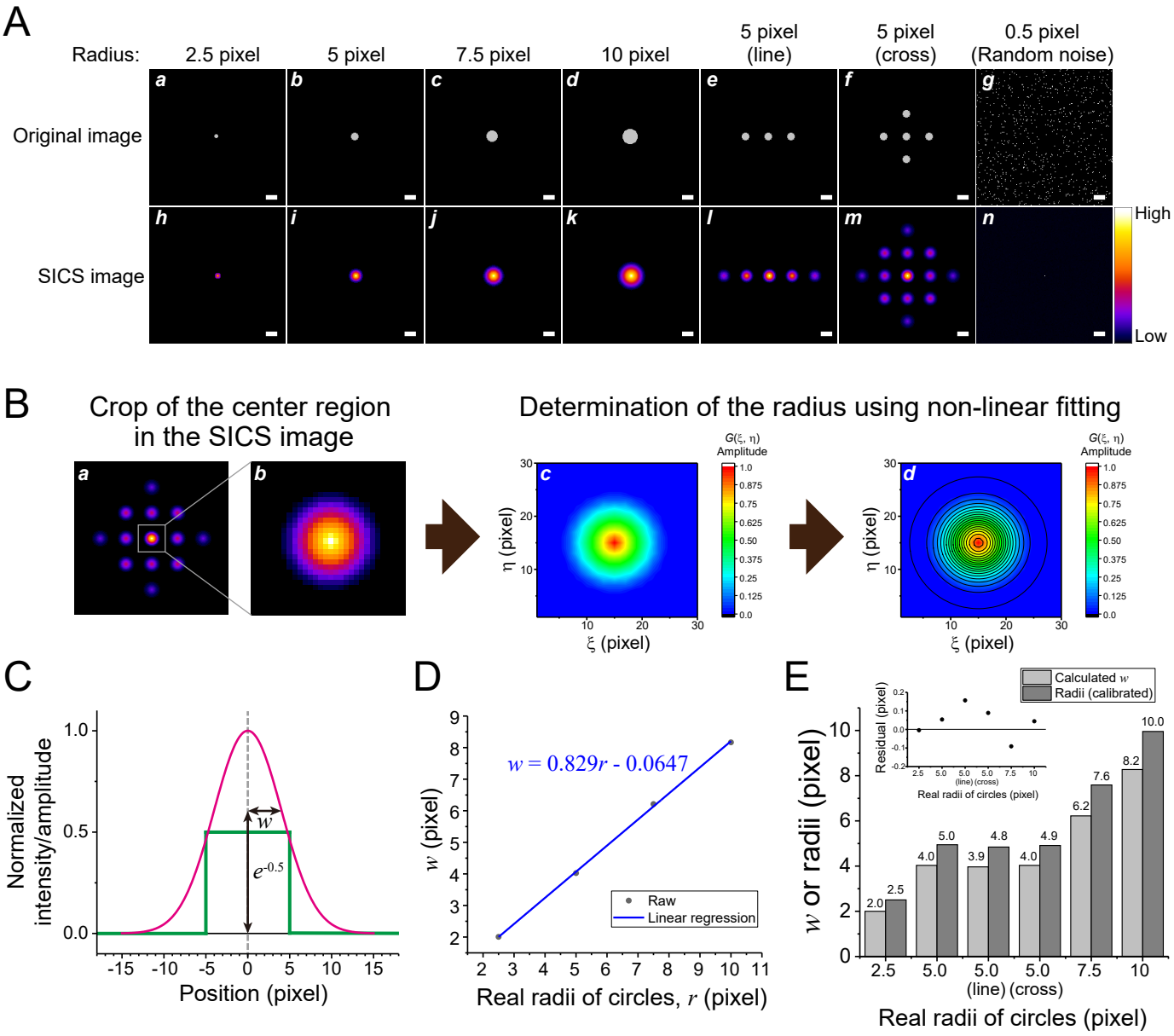
A
Radius:
2.5 pixel
5 pixel
7.5 pixel
10 pixel
5 pixel (line)
5 pixel (cross)
0.5 pixel (Random noise)
Original image
SICS image
High
Low
B
Crop of the center region in the SICS image
Determination of the radius using non-linear fitting
G(ξ, η) Amplitude
η (pixel)
ξ (pixel)
C
Normalized intensity/amplitude
Position (pixel)
w
e-0.5
D
w (pixel)
w = 0.829r - 0.0647
Raw
Linear regression
Real radii of circles, r (pixel)
E
Calculated w
Radii (calibrated)
Residual (pixel)
Real radii of circles (pixel)
w or radii (pixel)
(line) (cross)
Real radii of circles (pixel)

Figure 3

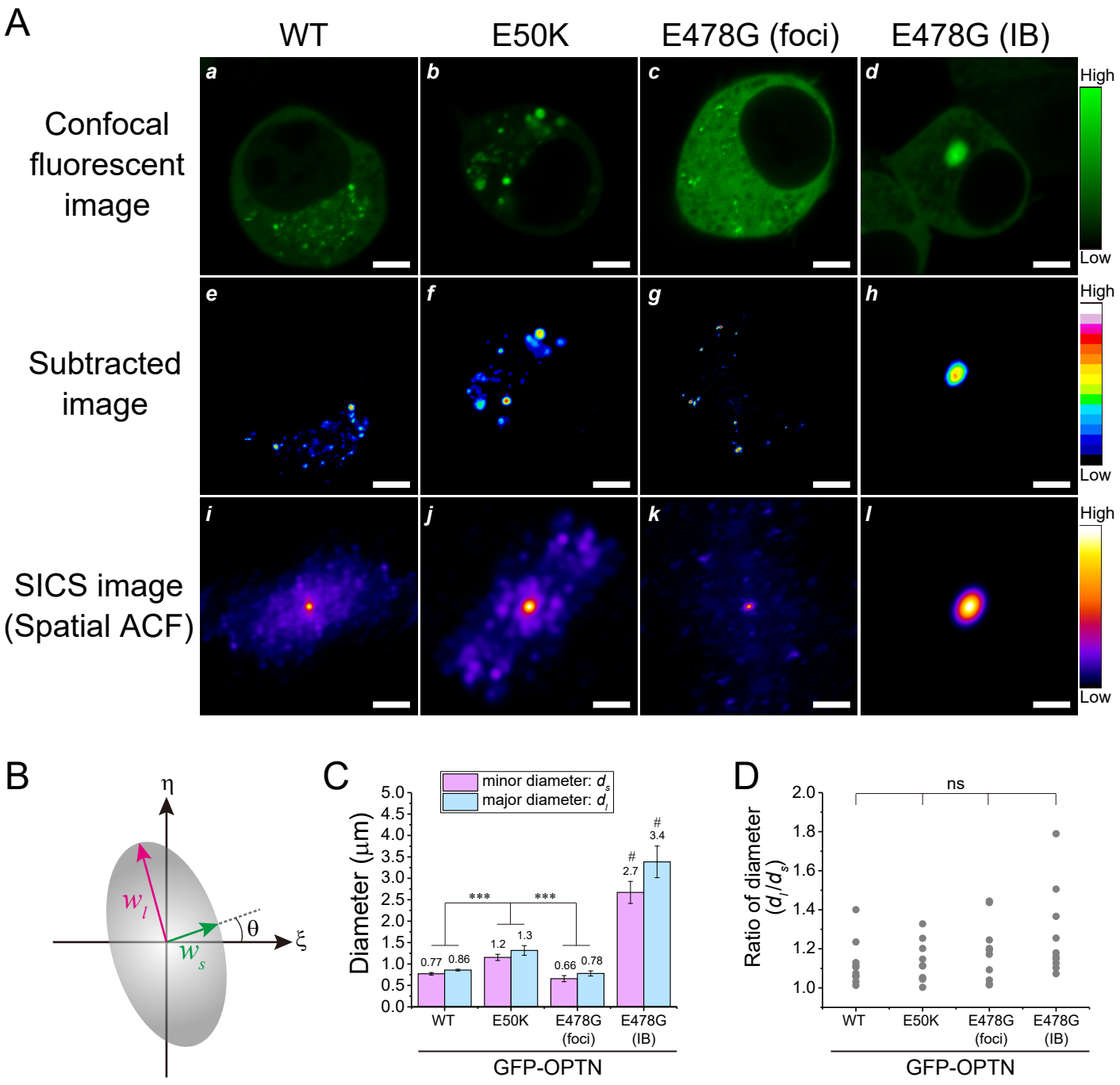
A
WT
E50K
E478G (foci)
E478G (IB)
Confocal fluorescent image
Subtracted image
SICS image (Spatial ACF)
a
b
c
d
e
f
g
h
i
j
k
l
High
Low
B
η
ξ
θ
w_l
w_s
C
minor diameter: d_s
major diameter: d_l
Diameter (μm)
0.77
0.86
1.2
1.3
0.66
0.78
2.7
3.4
***
***
#
#
WT
E50K
E478G (foci)
E478G (IB)
GFP-OPTN
D
Ratio of diameter (d_l/d_s)
ns
WT
E50K
E478G (foci)
E478G (IB)
GFP-OPTN

Supplemental Figure

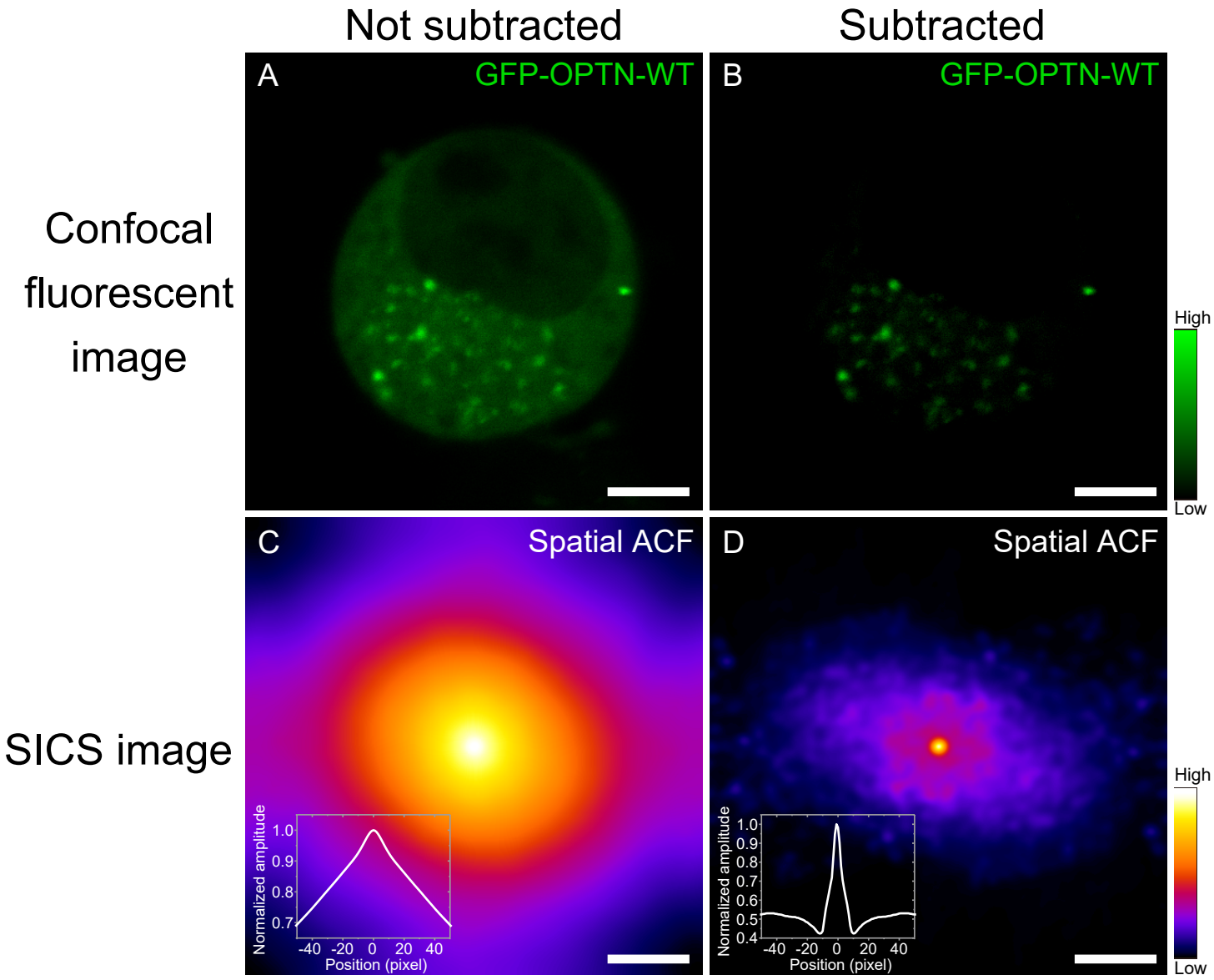

Supplemental Figure. Comparison of spatial autocorrelation function between cytoplasmic background-subtracted and non-subtracted image

Confocal fluorescence images of a Neuro2A cell expressing GFP-OPTN-WT (A & B), and calculated spatial autocorrelation function (ACF; C & D); bar = 5 μm. (B) Confocal fluorescence image after subtraction of mean intensity in the cytoplasmic region. (D) Spatial ACF of the subtracted image. Inset graph in C and D represents normalized amplitude of the spatial ACFs near the central coordinates.